Effect of preparation routes on the performance of a multi-component AB_2-type hydrogen storage alloy

Journal of Physics: Energy

PAPER

Effect of preparation routes on the performance of a multi-component AB_2-type hydrogen storage alloy

Moegamat Wafeeq Davids[1], **Tayla Chirie Martin**[1], **Pavel V Fursikov**[2], **Mikhail V Zhidkov**[3], **Igor I Khodos**[4], **Simbarashe Fashu**[5] **and Mykhaylo V Lototskyy**[1,2,*]

[1] HySA Systems Centre of Competence, University of the Western Cape, Bellville, South Africa
[2] Laboratory of Metal Hydride Energy Technologies, Federal Research Center of Problems of Chemical Physics and Medicinal Chemistry, Russian Academy of Sciences, Chernogolovka, Russia
[3] Laboratory of Physical Methods of Studying Functional Materials, Federal Research Center of Problems of Chemical Physics and Medicinal Chemistry, Russian Academy of Sciences, Chernogolovka, Russia
[4] Institute of Microelectronics Technology and High Purity Materials, Russian Academy of Sciences, Chernogolovka, Russia
[5] Department of Chemical Engineering, University of KwaZulu Natal, Durban, South Africa
* Author to whom any correspondence should be addressed.

E-mail: mlototskyy@uwc.ac.za

OPEN ACCESS

RECEIVED
16 April 2024

REVISED
13 June 2024

ACCEPTED FOR PUBLICATION
21 June 2024

PUBLISHED
3 July 2024

Keywords: hydrogen storage, metal hydride, high-entropy alloy, AB_2–type intermetallic, preparation routes

Supplementary material for this article is available online

Abstract

This article presents experimental results on the preparation and characterisation of a multi-component AB_2–type intermetallic hydrogen storage alloy ($A = Ti_{0.85}Zr_{0.15}$, $B = Mn_{1.22}Ni_{0.22}Cr_{0.2}V_{0.3}Fe_{0.06}$). The alloy samples were prepared by induction melting using Y_2O_3-lined alumo-silica and graphite crucibles. The characterisation results were compared with the ones for the reference sample of the same composition prepared by arc melting. It has been shown that the induction-melted samples exhibit reduced hydrogen sorption capacities and sloping plateaux on the pressure composition isotherms (PCI's). The origin of the observed effects has been shown to be in the inhomogeneity of the induction-melted alloys and their contamination due to crucible—melt interaction, particularly pronounced for the alloy melted in the alumo-silica crucible; this alloy was additionally characterised by the decrease of Zr/Ti ratio and, in turn, higher plateau pressures of the PCI's.

1. Introduction

Metal hydrides (MHs) able to reversibly and selectively interact with hydrogen both from a gas and an electrolyte are characterised by unique properties, including extremely high-volume density of H atoms accommodated in the metal matrix, reversibility and fast kinetics of hydrogenation/dehydrogenation, selectivity of hydrogen uptake, significant changes of physical properties of the host metal (alloy) in the course of its hydrogenation, catalytic activity in hydrogen transfer reactions. The MH technologies utilising these features can provide very efficient solutions, particularly in energy storage and conversion technologies [1–4].

Hydride forming materials represented by a vast number of Laves-type $AB_{2\pm x}$ intermetallics can reversibly interact with hydrogen in an extremely wide range of pressures. Their hydrogen sorption properties can be easily tuned in wide limits by a partial substitution of A- or B-component in a binary intermetallic compound or changing the B/A ratio. One example is C15-$ZrFe_2$ (plateau pressure above 700 bar at the ambient temperature) [5] and C14-$ZrFe_{2-x}V_x$ ($x = 0.25$–0.5) characterised by the plateau pressure at the same temperature far below the atmospheric one [6, 7]. Another example is C14-$TiMn_2$. This intermetallic has a huge hysteresis in the system with H_2 gas (absorption/desorption plateau pressure at $T = 25$ °C of 415/34 bar [8]), but the under-stoichiometric C14-$TiMn_{1.5}$ absorbs more than 1.7 wt.% H at $T = 20$ °C and $P < 45$ bar and exhibits desorption plateau pressure about 7 bar at the same temperature. The substitution of Ti with Zr in the stoichiometric alloy noticeably reduces the hydride stability (plateau

pressure below 0.1 bar at $T = 20$ °C for $Ti_{0.5}Zr_{0.5}Mn_2$) [9]. The variation of composition and stoichiometry of the multi-component Laves-phase intermetallics allows to further extend the range of hydrogen equilibrium pressures for their hydrides covering more than ten orders of magnitude at operating temperatures below 300 °C. These materials have been used in several applications, including hydrogen storage and compression, heat management, getters and low-pressure sources of hydrogen, as well as rechargeable nickel-MH batteries [10]. Wide tuneability of thermodynamic properties of hydrogen systems with the multi-component AB_2-type alloys where A = Ti + Zr and B = Mn + Cr + V + Fe by the variation of the alloy composition makes these materials very promising for compact hydrogen storage at near-ambient conditions and thermally-driven hydrogen compression to several hundred bars in the temperature range 20 °C–150 °C [11, 12].

We note that most of the multi-component hydrogen storage alloys belong to high-entropy alloys (HEAs) mainly represented by BCC solid solutions and/or C14-Laves phase intermetallics [13–15]. Suitable relationships between the hydride-forming (e.g. A = Ti, Zr, Hf; B = V, Nb) and non-hydride-forming (e.g. B = Mn, Cr, Fe, Co, Ni) components in the latter materials, along with the possibility to vary the key HEA's properties including mixing entropy and enthalpy, valence electron concentration, size and electronegativity mismatch, etc., opens wide opportunities for the tuning the alloys' composition towards matching with the requirements of their target hydrogen storage applications.

Preparation routes of the Ti- and Zr-based AB_2-type alloys include conventional metallurgical (smelting) and powder metallurgical (sintering, mechanical alloying) methods [10, 16]. Because of high inhomogeneity and uncontrolled contamination which result in poor reproducibility of hydrogen sorption performance of the final product prepared using the latter group of methods, the metallurgical methods based on melting the metallic components and further post-processing of the ingot (annealing, rapid solidification, etc) are preferred [10]. These methods mainly include arc-melting and induction melting [17]. The use of arc melting (with a non-consumable tungsten electrode and a water-cooled copper hearth) in the atmosphere of a purified inert gas allows to produce the highest purity ingots which are, however, highly inhomogeneous and require multiply re-melting and further annealing. This route is difficult to upscale and, as a rule, it is used in laboratories to prepare reference samples of the alloys.

Induction melting is more suitable for the upscaled manufacturing of the Ti- and Zr-based AB_2-type alloys. At the same time, due to the high solidification temperatures of these alloys, along with the high reactivity of Ti- and Zr-containing melts, the preparation of large amounts of these materials requires special care. The alloys prepared in laboratory conditions (arc melting and annealing) and manufactured using industrial-scale facilities (induction melting) often show differences in their structure, morphology and hydrogen sorption performances [17]. This effect has many origins, including non-uniformity of solidification, the concentration inhomogeneity, as well as the contamination of the ingot with the crucible material, also associated with the shortening of the crucible lifetime due to a crucible—melt interaction which may include capturing of oxygen from commonly used ceramic materials (e.g. Al_2O_3 or $Al_2O_3 + SiO_2$), or, when using crucibles made of graphite, formation of carbides or dissolution of carbon in the melt [10, 16, 18].

Thus, the induction melting of the AB_2-type alloys (A = Ti + Zr) requires the melting crucible to be carefully selected and designed to avoid melt contamination at high temperatures; the crucible should also have a high thermal shock resistance and relatively low cost [16, 19]. One of the effective ways to solve this problem is in the use of conventional crucibles (e.g., made of Al_2O_3) coated with a thin layer of yttrium oxide, which is one of the most resistant materials towards interaction with Ti-containing melts [20]. Earlier, we applied this route for the induction melting of $Ti_{0.85}Zr_{0.15}Mn_{1.2}M_{0.8}$ (M = V + Cr + Ni + Fe) AB_2-type hydrogen storage alloy and showed that the Y_2O_3 coating of alumo-silica and graphite crucibles prevents destruction of the crucible during the melting and allows to obtain suitable quality ingots [16].

In this work, we present further details on the preparation and results of characterisation of the multi-component AB_2–type hydrogen storage alloy to demonstrate the influence of preparation route on performance.

2. Experimental

2.1. Preparation of the samples

The high-entropy AB_2 type hydrogen storage alloy (A = $Ti_{0.85}Zr_{0.15}$, B = $Mn_{1.22}Ni_{0.22}Cr_{0.2}V_{0.3}Fe_{0.06}$; mixing entropy of the components $\Delta S_{mix} = 12.92$ J/(g-at.M K) = 1.55 R, i.e. above the threshold of 1.5 R for the HEAs [13, 14]; the mixing enthalpy $\Delta H_{mix} = -11.41$ kJ/g-at M) was intended for the use for hydrogen storage on board fuel cell vehicle at near-ambient temperatures [21]. The alloy was prepared by induction melting of the metallic components under Ar atmosphere. The starting components were all purchased from South African suppliers with a purity of >98%; these included electrolytic Mn (low oxygen flake), Ti (grade

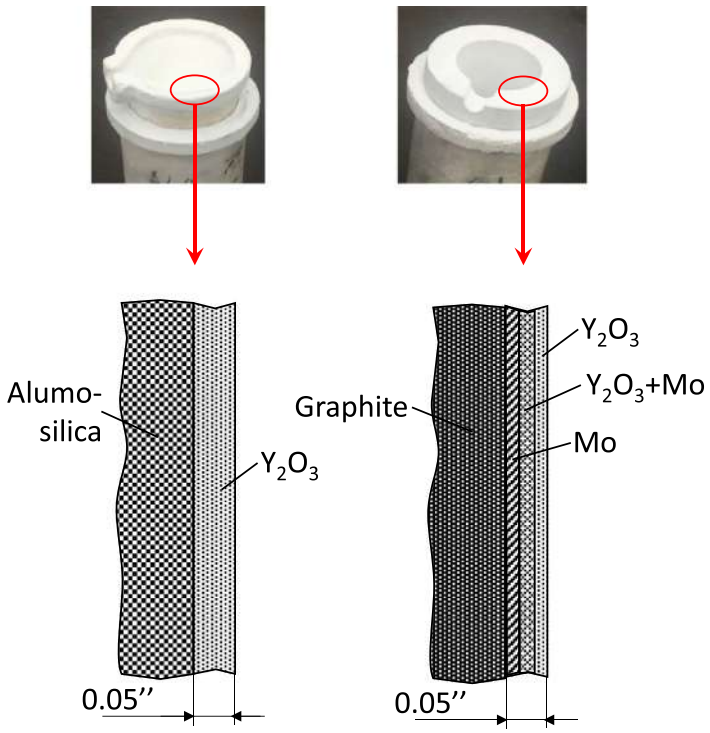

Figure 1. Images and schematic cross-sections of the Y_2O_3-coated crucibles.

2, cut-offs), Zr (sponge), Cr (pieces), Ni (powder), and Ferrovanadium (powder; 80 wt.% V). 1 wt.% La was added to the charge to assist with the activation of the alloy according to the recommendation found in [22].

The samples ($m = 100$ g) were prepared in SM 10 K VHT vacuum induction melting furnace with a crucible capacity of 200 g. Two types of crucibles were used: ceramic alumo-silica ($Al_2O_3 + SiO_2$) and graphite, ~150 g in weight each. Each crucible was placed into alumo-silica crucible of the bigger size (see top images in figure 1).

To minimise interaction between the melt and the crucible material, both crucibles were coated inside by the deposition of a protective coating whose surface contacting the melt was yttria (Y_2O_3). In both cases, the total coating thickness was of 0.05 inches (see figure 1, bottom).

The alumo-silica crucible was directly spray-painted with Y_2O_3 slurry—pure yttria powder suspended in 5% aqueous solution of caboxylmethylcellulose (CMC) stabiliser. The coated crucible was dried in an oven at $T = 80$ °C.

The coating of the graphite crucible had three layers, which were shown to provide good adhesion of the external Y_2O_3 refractory layer to the graphite substrate. The inner molybdenum metallic layer was applied as a diffusion barrier to carbon, and the intermediate Mo + Y_2O_3 layer was used to absorb thermal shocks. Spray painting was used to first coat Mo slurry (powder with particle size below 5 μ suspended in the CMC solution), then Mo + Y_2O_3 slurry, and finally Y_2O_3 slurry, with drying in an oven after each stage at T = 80 °C. The CMC was vaporized during pre-heat of the crucible before the melting.

The charge was loaded into the Y_2O_3 lined alumo-silica- or graphite-based crucible, which was then placed into the vacuum furnace chamber, followed by flushing the chamber three times by evacuation to 10^{-3} mbar and Ar refilling (0.3–1 bar). After flushing, the vacuum furnace chamber was filled with Ar (1 bar), and the electric power supplied to the inductor was gradually increased until the complete melting of the charge was visually observed. The charge was maintained in the molten state at $T = 1600$ °C–1800 °C for 1 min. After solidification in the crucible and cooling to ambient temperature, the ingot could be easily removed [16].

The reference sample of the same composition ($m = 10$ g) was prepared by arc-melting performed on a water-cooled copper hearth in Ar atmosphere (99.999%; pressure 1 bar). The alloy was turned over and re-melted three times to provide the ingot homogeneity.

2.2. Characterisation of the samples

The composition, morphology and the degree of crystallinity of the AB_2 alloy samples were studied by SEM/EDS (Zeiss Auriga scanning electron microscope) and TEM/SAED (JEOL JEM-2100 transmission

electron microscope operating at 200 kV). For the SEM/EDS analyses, the sample powders were mounted onto fresh carbon discs. The samples for TEM/SAED studies were prepared by the deposition of the sample powder, using ultrasonic dispersant, onto a substrate (copper mesh covered with electrically conductive amorphous film).

The studies of the elemental composition of the alloys were supplemented by atomic emission spectroscopy (AES) for the detection of impurities using a laser analyser LEA-S500 (SOL Instrument). Improvement of the resolution of the impurity spectral lines overlapping with the ones for the metallic components was achieved by optimising the energy of laser irradiation impulse in the range between 18 and 21.5 J.

The alloys phase composition was determined by XRD (Rigaku Minflex diffractometer) using Cu–K_α radiation ($\lambda_1 = 1.5406$ Å, $\lambda_2 = 1.5444$ Å, $\lambda_2/\lambda_1 = 0.5$, $2\theta = 15$–$90°$). The XRD data was further processed by Rietveld full-profile analysis using GSAS software [23] and the following reference data:

- C14-AB_2 Laves phase intermetallic ($Ti_{0.95}Zr_{0.05}Mn_2$): space group $P6_3/mmc$ (194), $a = 4.826$ Å, $c = 7.921$ Å, unit cell volume 159.8 Å^3 [24];
- (Ti,Zr)O_2 mixed oxide: space group $Pbcn$ (60), $a = 4.7447$ Å, $b = 5.0119$ Å, $c = 5.4925$ Å [25];
- La_2TiO_5: space group $Pnma$ (62), $a = 11.0092$ Å, $b = 3.9433$ Å, $c = 11.4063$ Å [26].

A standard α-Al_2O_3 sample was used to determine the instrumental contribution into peak profile parameters. During refinements, the Gaussian profile parameters (GU, GV and GW) were fixed (kept the same as for the Al_2O_3 standard), and only two Lorentzian profile parameters were refined, LX (size broadening) and LY (strain broadening).

Further details about the XRD studies are presented in supplementary information, section S1.

The pressure–composition isotherms (PCI) of the samples were measured using a commercial automated Sievert-type apparatus (PCT Pro-2000). Approximately 1 g of the sample was loaded into the reactor; the sample was then activated by heating to 300 °C under dynamic vacuum for 1 h. The sample was then allowed to cool down to ambient temperature, followed by charging with hydrogen at the starting H_2 pressure above 30 bar. The hydrogen absorption and desorption isotherms were recorded at the temperatures of 20, 40 and 60 °C and hydrogen pressures from 0.1 to 100 bar.

3. Results and discussion

3.1. SEM and EDS

The SEM images of the AB_2 type alloy samples prepared by the different routes (figure 2) show that there are no visual differences between the alloys prepared by arc and induction melting: all the alloys exhibit a smooth, continuous surface. The EDS results (table 1) show that the measured amounts of the metallic components are in satisfactory correspondence with the nominal composition of the alloy. However, for the induction melted samples several deviations were observed. Mainly, it relates to the underestimation of Zr content in the alloy induction-melted in alumo-silica crucible.

No impurities were detected in the arc-melted alloy, while both alloys prepared by induction melting contained oxygen (O) impurities. The presence of oxygen can be attributed to the contamination of the sample with Y_2O_3 particles from the crucible coating (most probable reason for the sample melted in the graphite crucible where oxygen was detected only in a few separate points), as well as to the interaction of the melt with the residual atmosphere of the induction furnace chamber and with the inner surface of the crucible. The latter also relates to the source of the silicon (Si) impurity, which was found only in the sample prepared in the alumo-silica crucible.

The EDS results allow us to conclude that the applied protecting coating, which eliminates severe contamination of the ingot and destruction of the crucible due to its interaction with the melt [16] does not result in the complete elimination of the latter process accompanied by the leaching of some metallic components and contamination of the ingot with non-metallic impurities. However, this effect is much less pronounced for the graphite crucible.

Due to interference with the background signal from carbon support, the reliable determination of carbon in the studied samples by EDS was not possible.

3.2. XRD

The refined XRD patterns of the alloy samples (background subtracted) are presented in figure 3. Results of the Rietveld refinement of the as-measured patterns are shown in supplementary information (figures S1–S3) and summarised in table 2 where calculated abundancies and lattice periods of the constituent phases, along with the unit cell volumes for the major C14-AB_2 phase, are presented. The last column in

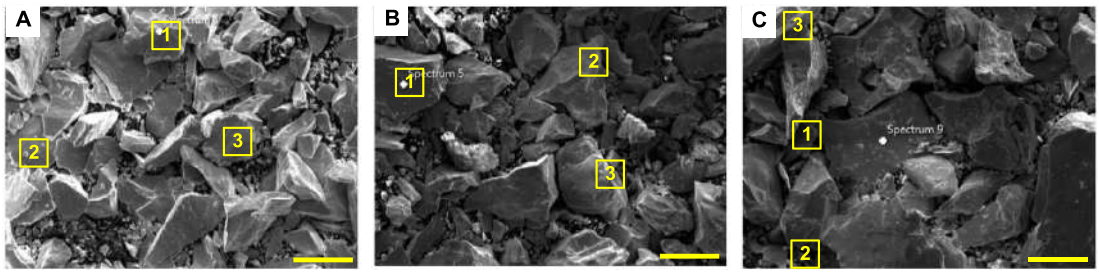

Figure 2. SEM images of the AB_2-type alloy prepared by (A)—arc-melting and annealing, (B)—induction melting in alumo-silica crucible, and (C)—induction melting in graphite crucible. Each scale bar (thick yellow line) corresponds to 100 μm.

Table 1. Summary of compositional properties of the alloy samples according to EDS data collected from typical points (1–3 in figure 2).

		Content (wt. %)											
		Measured: figure 2(A) Arc melted				Measured: figure 2(B) induction melted (alumo-silica crucible)				Measured: figure 2(C) induction melted (graphite crucible)			
Components	Nominal	Total area	Point 1	Point 2	Point 3	Total area	Point 1	Point 2	Point 3	Total area	Point 1	Point 2	Point 3
A (Ti)	26.38	25.10	24.26	26.57	23.74	25.5	24.82	24.85	23.93	28.25	25.65	25.51	28.73
A (Zr)	8.38	8.61	9.19	8.83	8.80	7.30	5.16	4.93	9.09	8.30	9.95	8.48	6.45
B (Cr)	6.82	6.77	6.90	6.20	6.50	7.66	7.46	8.18	8.17	7.25	6.70	6.98	6.90
B (Mn)	40.76	41.19	41.82	39.84	42.60	42.44	43.16	42.93	41.69	40.25	43.08	41.67	40.34
B (Ni)	6.21	6.45	6.69	6.64	6.01	5.14	5.19	4.95	6.08	4.42	4.45	5.84	6.53
B (V)	9.47	9.81	9.34	10.09	9.99	9.30	10.32	11.07	8.54	9.29	8.14	7.50	7.51
B (Fe)	1.98	2.08	1.80	2.08	2.36	1.92	1.95	1.99	1.73	2.24	2.03	2.15	1.88
Impurity (O)						2.24	0.67	0.59	0.11			1.87	1.66
Impurity (Si)						0.42	0.39	0.51	0.66				

table 2 also presents the estimations of the crystallite size of the constituent phases calculated from the LX profile parameter (see section 2.2). It has to be noted that the presented values are only rough estimations because, for the major C14-AB_2 phase in the arc melted and induction-melted in graphite crucible samples, the calculated crystallite size exceeds or approaches the value of 100–200 nm above which the precision of the size calculations from XRD data drops dramatically [27, 28]. Nevertheless, this observation testifies about high degree of crystallinity of the major phase in these samples further confirmed by the TEM/SAED studies (section 3.3) while the impurity phases have a nanocrystalline nature.

It is seen from table 2 that the sample prepared by arc melting is single-phase, which is in line with the EDS results (table 1). In La-containing induction-melted samples, La_2TiO_5 formed during interaction of La deoxidiser with molten Ti and oxygen was detected. In the sample induction-melted in alumo-silica crucible main impurity phase was found to be the $(Ti,Zr)O_2$ mixed oxide characterised by broad peaks testifying about nanocrystalline nature of this impurity.

The lattice periods and unit cell volumes of the major C14-AB_2 phase in the studied samples are higher as compared to the reference data [25]; the increase of the unit cell volume for the arc melted alloy was of 3.81% at the similar *c*/*a* ratio (1.637 against 1.641 for the studied and reference samples, respectively). The increase in the lattice periods is caused by the higher content of zirconium (atomic radius[6] 1.60 Å) in the studied alloy as compared to the reference intermetallic mainly containing Ti (atomic radius 1.46 Å).

When comparing the unit cell volume of the major phase in the arc melted and induction melted alloys, it can be seen that for the alloy melted in alumo-silica crucible, it is reduced by 0.91% while increases by 0.71% for the alloy melted in the graphite crucible. The smaller lattice periods and unit cell volume for the sample induction melted in alumo-silica crucible can be explained by the reduced content of Zr in this alloy (see section 3.1). The reason for the increase of the lattice periods of the C14-AB_2 phase in the sample induction melted in the graphite crucible is less clear. Presumably, it could be explained by the presence of interstitial carbon in this sample.

[6] When considering atomic radii of the elements, we mean the values which correspond to their coordination numbers in Laves phase intermetallics equal to 16 and 12 for A-and B-components, respectively [29].

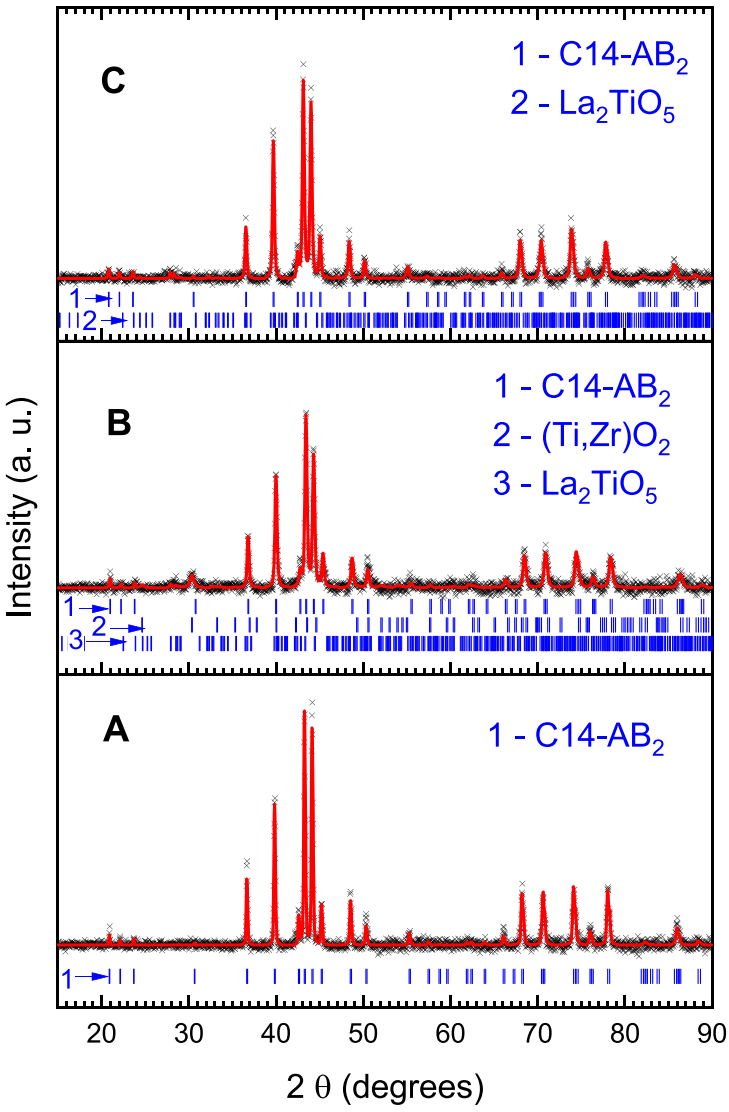

Figure 3. Observed (points) and calculated (red lines) XRD patterns of the AB_2-type alloy prepared by (A)—arc-melting, (B)—induction melting in alumo-silica crucible, and (C)—induction melting in graphite crucible. Bottom ticks show the calculated peak positions of the constituent phases.

Table 2. Summary of Rietveld refinement of the XRD patterns of the studied alloy samples (figure 3). Errors of the values calculated during refinement (shown in brackets) relate to the last decimal digit.

Alloy composition preparation method	Phase	Abundance (wt. %)	Lattice periods (Å)			Unit cell volume (Å^3)	Estimated crystallite size (nm)
			a	*b*	*c*		
$Ti_{0.85}Zr_{0.15}Cr_{0.2}Mn_{1.22}Ni_{0.22}V_{0.3}Fe_{0.06}$ Arc melting	C14-AB_2	100(−)	4.8910(1)	—	8.0063(3)	165.868(8)	>200
$Ti_{0.85}Zr_{0.15}Cr_{0.2}Mn_{1.22}Ni_{0.22}V_{0.3}Fe_{0.06}$ + 1 wt% La Induction melting in alumo-silica crucible	C14-AB_2	87.9(−)	4.8765(2)	—	7.9810(6)	164.37(2)	80
	$(Ti,Zr)O_2$	10.2(6)	4.86(1)	5.38(1)	5.08(1)		25
	La_2TiO_5	1.9(3)	10.90(5)	3.93(1)	11.43(4)		50
$Ti_{0.85}Zr_{0.15}Cr_{0.2}Mn_{1.22}Ni_{0.22}V_{0.3}Fe_{0.06}$ + 1 wt% La Induction melting in graphite crucible	C14-AB_2	98.0(−)	4.9019(1)	—	8.0290(4)	167.08(1)	100
	La_2TiO_5	2.0(3)	10.80(2)	3.952(5)	11.58(2)		80

3.3. TEM, SAED and AES

The TEM images and selected area electron diffraction (SAED) patterns taken from the areas containing several alloy particles are shown in figure 4. The patterns exhibit the presence of both rings and spots, signifying that the alloys are mainly polycrystalline in nature. However, all the samples exhibit the presence of

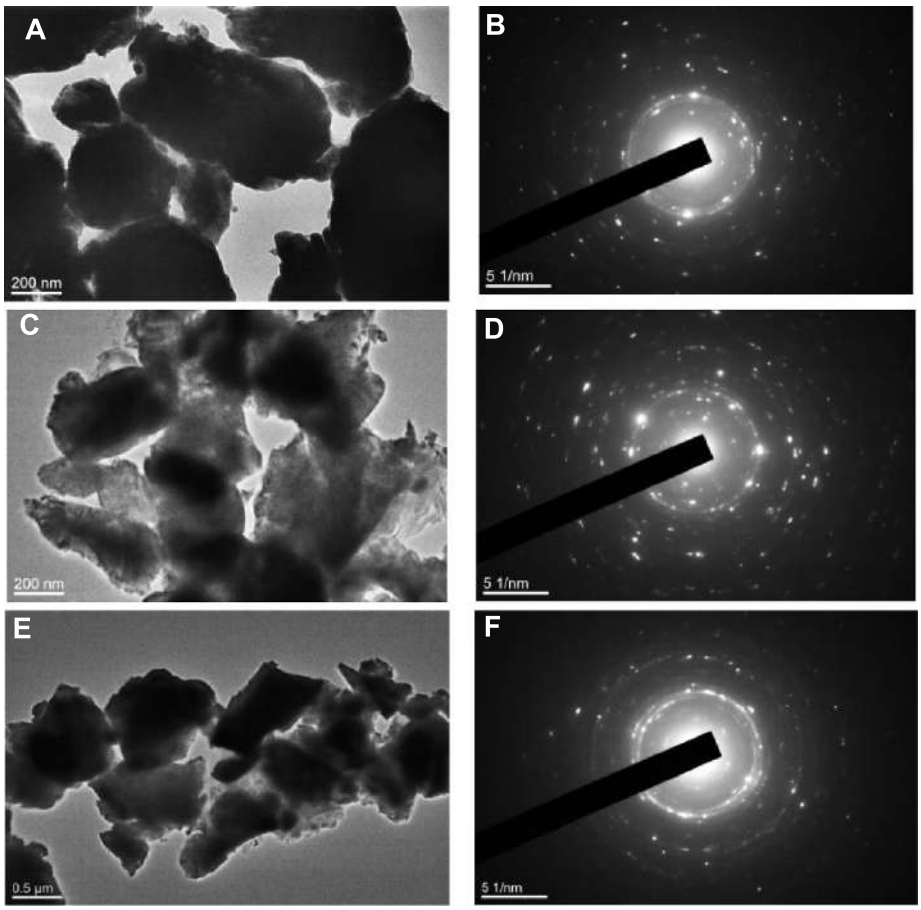

Figure 4. TEM images (A), (C), (E) and the corresponding SAED patterns (B,D,F) for the arc-melted sample (A), (B), the sample induction melted in the alumo-silica crucible (C), (D) and the sample induction melted in the graphite crucible (E), (F).

separate, almost completely monocrystalline particles (figure 5), which for the sample melted in the graphite crucible (E, F) have the highest degree of crystallinity. This sample also does not contain completely polycrystalline separate particles, which were found in other samples. The reason for these observations appears to be due to the slower cooling rate of this sample since both the electrically conductive graphite crucible and the sample were heated during induction melting, therefore the hot mass (100 g of the sample and 150 g of graphite) will cool down slower than in the case of alumo-silica crucible (100 g of sample only) at the similar cooling conditions. Conversely, very fast cooling of the sample during arc melting may result in a slightly poorer crystallinity; see figures 5(A) and (B). For the sample induction melted in alumo-silica crucible and characterised by the poorest crystallinity (see figures 5(C) and (D)), the origins of the observed effect may also be in the presence of noticeable amounts of impurity phases, including nanocrystalline $(Ti,Zr)O_2$ (see XRD data in table 2) which was not detected in the SAED patterns, as well as introducing silicone into metallic matrix (see table 1) associated with appearance of additional lattice defects.

The SAED patterns for all the samples exhibit the presence of the major phase C14-AB_2 in good correspondence with XRD results (table 2), as illustrated by the example in figures 6(A) and (B) for the sample melted in alumo-silica crucible.

Of the impurity phases, only traces of La_2TiO_5 poorly crystallised monocrystals were found in the induction-melted samples (figure 6(C)). The low probability of occurrence of the corresponding reflections in SAED patterns taken from an area of $\sim$1 μ in diameter (figure 6(A)) is caused by the small content of this phase in the sample ($\leqslant$2 wt.% according to the XRD data).

Further details about TEM and SAED studies are presented in section S2 of supplementary information.

The AES studies gave a semi-quantitative validation of the EDS (table 1) and XRD (table 2) results, according to which the main impurity in the induction-melted samples was oxygen. It is illustrated by figure 7. The maximum amount of the oxygen impurity was determined for the sample induction melted in alumo-silica crucible, followed by the sample induction melted in graphite crucible and the arc melted sample. Additionally, the sample induction melted in alumo-silica crucible showed the presence of aluminium impurity that, along with the presence of silicon in the ingot, confirms our assumption about

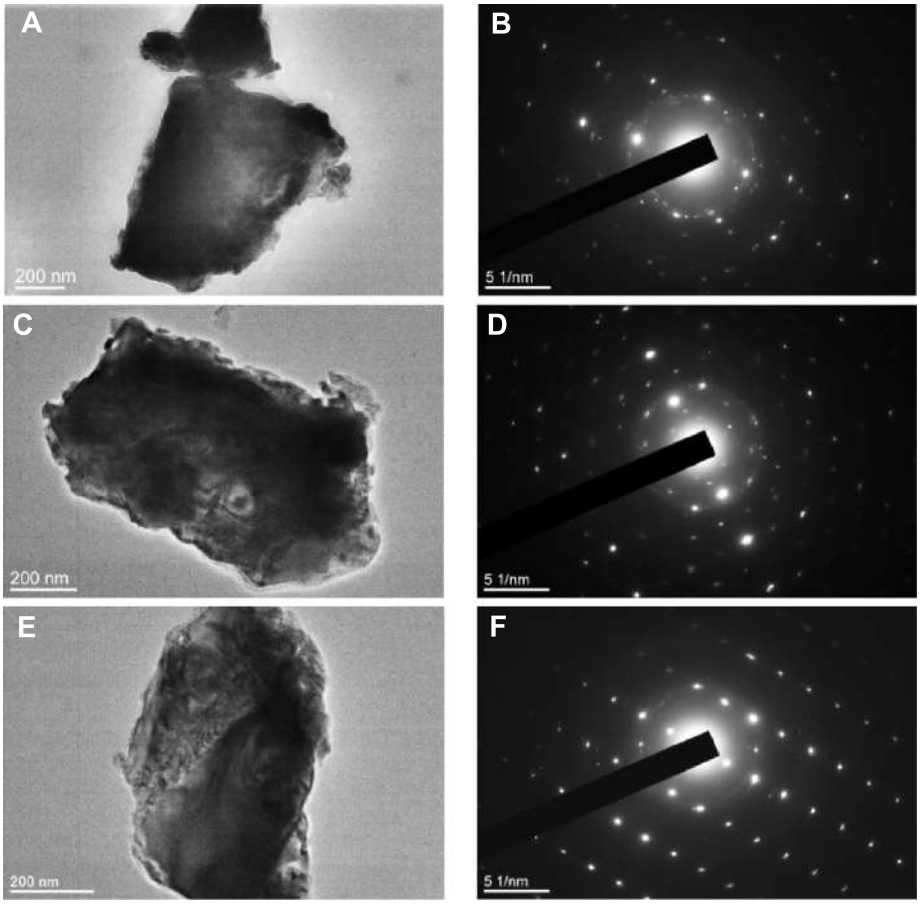

Figure 5. TEM images (A), (C), (E) and the corresponding SAED patterns (B), (D), (F) of separate particles for the arc-melted sample (A), (B), the sample induction melted in the alumo-silica crucible (C), (D) and the sample induction melted in the graphite crucible (E), (F).

incomplete elimination of the crucible—melt interaction by the protective Y_2O_3 coating, at least, for the alumo-silica crucible (section 3.1).

Due to the overlapping of the most intensive carbon line (247.8561 nm) with the lines of Fe, Cr and Ti, it could not be resolved during AES studies. We assume that all three samples do not contain noticeable amounts of carbon, but presence of its traces in the sample melted in graphite crucible is possible.

3.4. Hydrogen sorption properties

Figure 8(A) shows the as-measured hydrogen absorption and desorption isotherms ($T = 20$ °C) for the studied alloy samples. The corresponding van't Hoff plots at H/M = 0.35 are shown in figure 8(B), and the main hydrogen sorption parameters taken from the pressure—composition isotherms are summarised in table 3.

As it can be seen, the induction melted samples exhibit significant reduction in both maximum and reversible hydrogen storage capacity, especially pronounced for the sample induction melted in alumo-silica crucible. This sample (# 2 in figure 8) is also characterised by the lowest thermal stability of hydride, resulting in the higher hydrogen equilibrium pressures. The latter effect can be explained by the lower content of the zirconium in this sample (section 3.1), which also results in the decrease of the lattice periods and the unit cell volume of the C14-AB_2 major phase (section 3.2). The decrease of the maximum hydrogen storage capacity (~82% as compared to the one for the arc melted alloy; table 3) also correlates well with the minimum abundance of this phase as shown by XRD (~88%; table 2) where the impurity phases do not absorb hydrogen. Thus, we can conclude that during induction melting in the alumo-silica crucible, even protected by Y_2O_3 coating, the crucible—melt interaction, along with oxygen contamination, results in the predominant removal from the melt of Zr characterised by higher than Ti affinity to oxygen [16].

The induction melted samples are also characterised by the increased plateau slope, which is especially pronounced for the sample melted in the graphite crucible. This effect can be associated with the inhomogeneity of these samples. An additional reason may be in the incorporation of the traces of non-metallic impurities into interstitials of the C14-AB_2 major phase. Such effects for boron and carbon

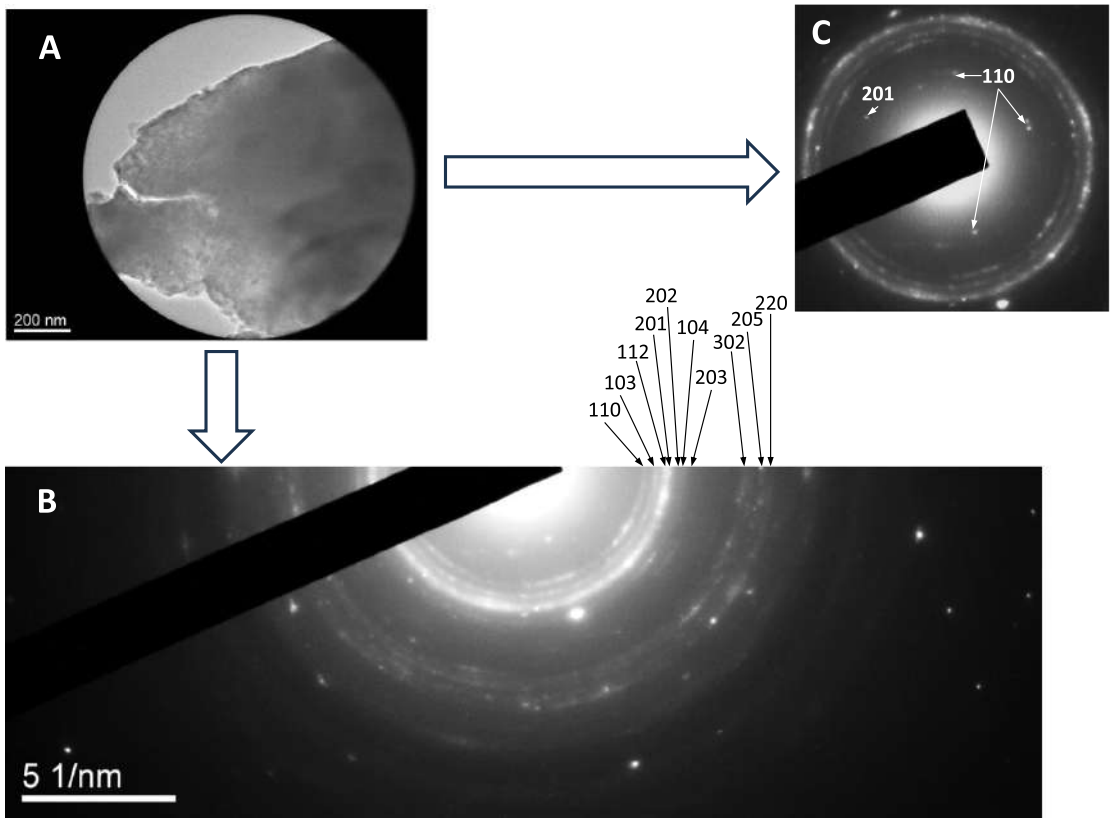

Figure 6. Selected area of the TEM image (A) taken for the sample induction melted in alumo-silica crucible and the corresponding SAED patterns supplemented by Miller indexes of rings and spots for the major C14-AB_2 phase (B) and La_2TiO_5 impurity (C).

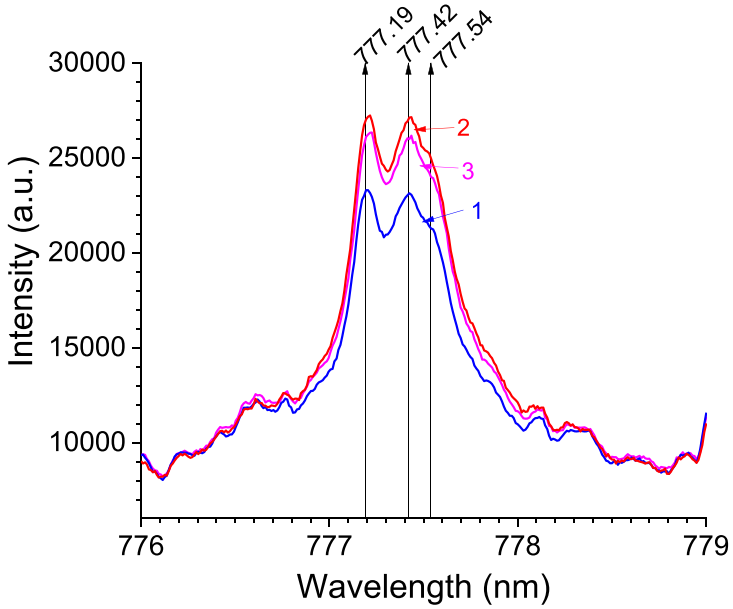

Figure 7. Fragments of atomic emission spectra for the arc-melted sample (1) and samples induction melted in alumo-silica (2) and graphite (3) crucible. The most intensive oxygen spectral lines are shown by the vertical arrows.

were observed for TiFe accompanied by a drastic decrease in hydrogen sorption capacity and increase in the plateau slope [18].

We note that despite significantly more incline plateau for the sample induction melted in the graphite crucible, the thermal stability of its hydride is very close to the one for the arc melted sample (figure 8(B), table 3).

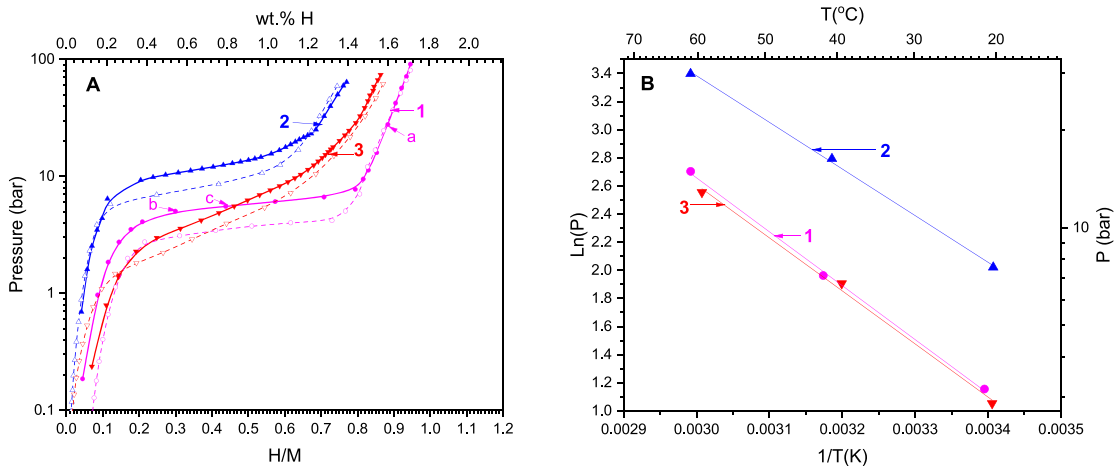

Figure 8. Hydrogen absorption and desorption isotherms at T = 20 °C (A) and van't Hoff plots for the AB_2-type alloy samples (B): (1)—arc melted, (2)—induction-melted in alumo-silica crucible and (3)—induction-melted in graphite crucible. Points a, b and c on the absorption isotherm for the arc melted sample (1 in A) correspond to hydrogen pressures and concentrations for which kinetic data (figures 9(A) and (B)) are presented.

Table 3. Hydrogen sorption parameters of the studied alloy samples.

Parameter		Sample		
		Arc melted	Induction melted in alumo-silica crucible	Induction melted in graphite crucible
H sorption capacity (H/M/wt.% H)	Maximum (absorption at $T = 20$ °C, $P = 50$ bar)	0.92/1.64	0.75/1.36	0.83/1.50
	Reversible (absorption at $T = 20$ °C, $P = 15$ bar, desorption at $T = 60$ °C, $P = 5$ bar))[a]	0.76/1.37	0.50/0.89	0.58/1.03
Thermodynamic parameters of hydride formation	$-\Delta H^o$ (kJ/mol H_2)	31.88	27.59	31.39
	$-\Delta S^o$ (J/(mol H_2 K))	117.74	111.07	115.85
	Hysteresis at $T = 20$ °C, $Ln(P_A/P_D)$	0.488	0.368	0.297
	Plateau slope at $T = 20$ °C, d(Ln P)/d(H/M)	0.991	1.227	3.363

[a] —typical conditions for the integrated energy systems comprising PEM electrolyser and PEM fuel cell.

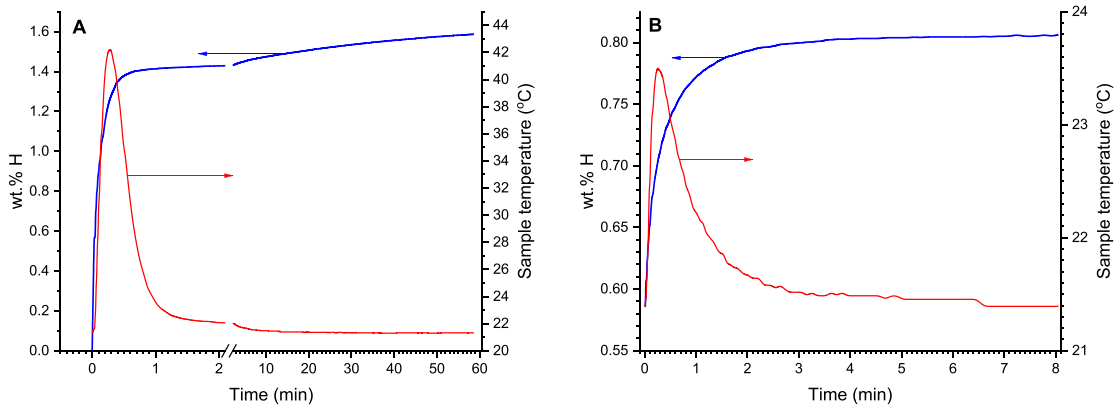

Figure 9. Hydrogen absorption kinetics and changes of the sample temperature at $T_0 = 21$ °C for the arc melted sample: (A)—first absorption at the starting H_2 pressure of 33 bar and final H_2 pressure of 27 bar (point a in figure 8(A)). (B)—hydrogen absorption during the measurement of the pressure–composition isotherm (points b and c in figure 8(A)).

All the alloys are characterised by a moderate hydrogen absorption desorption hysteresis, $Ln(P_A/P_D) = 0.3$–0.5, or hysteresis energy loss, RT $Ln(P_A/P_D) = 0.75$–1.25 kJ/mol H_2. Hysteresis slightly decreases in the series: arc melted → induction melted in alumo-silica crucible → induction melted in graphite crucible.

All the studied samples exhibit excellent hydrogen absorption and desorption kinetics. Typical example for the hydrogen absorption in the arc melted sample is shown in figure 9. As it can be seen from figure 9(A),

even the first H_2 absorption after vacuum heating is very fast: the equilibrium corresponding to point *a* in figure 8(A) is achieved in 1 h while about 90% of hydrogen is absorbed during the first 2 min accompanied by significant self-heating the sample due to exothermic nature of the hydrogenation process. Similar behaviour was observed during the measurements of the pressure–composition isotherms characterised by the low pressure driving force. It is illustrated by figure 9(B) which shows hydrogen absorption kinetics for the same alloy when passing from point *b* to point *c* on the absorption isotherm (figure 8(A)). The equilibrium is achieved in less than 10 min, and 95% of hydrogen is absorbed in 2 min.

4. Conclusions

This work has confirmed the high sensitivity of hydrogen sorption properties of AB_2-type hydrogen storage alloys (A = Ti + Zr) to their preparation routes, particularly when moving from arc melting to induction melting. The changes observed for the induction-melted alloys include lowering the hydrogen storage capacity and increasing the plateau slope mainly associated with the crucible—melt interaction accompanied by contamination of the ingot. Another reason for the observed effects is the higher inhomogeneity of the induction-melted alloys.

The crucible—melt interaction, which cannot be completely suppressed by the protective 0.05 inches-thick coating of the alumo-silica crucible deposited by spray-painting of suspension of Y_2O_3 powder, results in the contamination of the ingot with the components of the crucible material (oxygen, silicon, aluminium) and simultaneous leaching of zirconium (having the strongest affinity to oxygen) from the melt. As a result of the latter process, thermal stability of the formed hydride significantly decreases, leading to further decrease of the hydrogen sorption capacity of the alloy at the applied temperatures and hydrogen pressures.

The alloy induction melted in the graphite crucible which was protected by a three-layer coating of the same thickness where the outer layer was Y_2O_3 exhibited the lesser reduction of the hydrogen sorption capacity, and the hydride stability was very close to the one for the arc melted alloy. However, this alloy was characterised by the highest plateau slope, presumably originating from the incorporation of trace amounts of carbon into interstitials of the matrix of the major C14-AB_2 Laves phase.

This study has shown that selecting crucibles and looking for ways to suppress the crucible—melt interaction is essential in the preparation of MH alloys containing Ti and Zr by induction melting. Further studies should be aimed at the optimisation of the protective coating of graphite crucibles due to the lesser deterioration of the hydrogen sorption properties of the alloy prepared by induction melting in this crucible as compared to the arc melted one. An important stage of these activities would be in further clarifying the mechanisms of the ingot contamination and related deterioration of its hydrogen sorption performance.

Data availability statement

All data that support the findings of this study are included within the article (and any supplementary files).

Acknowledgments

The work of South African co-authors (sections 1, 2, 3.1, 3.2, 3.4 and 4) was supported by the Department of Science and Innovation of South Africa within HySA Program, Key Project KP6-S01. MWD also acknowledges support of National Research Foundation (NRF) of South Africa (Grant Number 141962).

The work of Russian co-authors (sections 1, 2.2, 3.3 and 4) was funded by the Ministry of Science and Higher Education of the Russian Federation (Megagrant, Agreement Number 075-15-2022-1126).

ORCID iDs

Moegamat Wafeeq Davids https://orcid.org/0000-0002-5057-1499
Mykhaylo V Lototskyy https://orcid.org/0000-0001-8387-2856

References

[1] Hirscher M *et al* 2020 Materials for hydrogen-based energy storage—past, recent progress and future outlook *J. Alloys Compd.* **827** 153548
[2] Pasquini L *et al* 2022 Magnesium- and intermetallic alloys-based hydrides for energy storage: modelling, synthesis and properties *Prog. Energy* **4** 032007
[3] Dornheim M *et al* 2022 Research and development of hydrogen carrier based solutions for hydrogen compression and storage *Prog. Energy* **4** 042005
[4] Lototskyy M V, Tarasov B P and Yartys V A 2023 Gas-phase applications of metal hydrides *J. Energy Storage* **72** 108165

[5] Sivov R B, Zotov T A and Verbetsky V N 2011 Hydrogen sorption properties of ZrFex (1.9 ⩽ x ⩽ 2.5) alloys *Int. J. Hydrog. Energy* **36** 1355–8
[6] Ivey D G and Northwood D O 1986 Storing hydrogen in AB2 laves-type compounds *Z. Phys. Chem.* **147** 191–209
[7] Yadav T P, Shahi R R and Srivastava O N 2012 Synthesis, characterization and hydrogen storage behaviour of AB_2 ($ZrFe_2$, $Zr(Fe_{0.75}V_{0.25})_2$, $Zr(Fe_{0.5}V_{0.5})_2$ type materials *Int. J. Hydrog. Energy* **37** 3689–96
[8] Klyamkin S N, Verbetsky V N and Demidov V A 1994 Thermodynamics of hydride formation and decomposition for TiMn2-H2 system at pressure up to 2000 atm *J. Alloys Compd.* **205** L1–2
[9] Gamo T, Moriwaki Y, Yanagihara N, Yamashita T and Iwaki T 1985 Formation and properties of titanium-manganese alloy hydrides *Int. J. Hydrog. Energy* **10** 39–47
[10] Yartys V A and Lototskyy M V 2022 Laves type intermetallic compounds as hydrogen storage materials: a review *J. Alloys Compd.* **916** 165219
[11] Pickering L, Lototskyy M V, Davids M W, Sita C and Linkov V 2018 Induction melted AB2-Type metal hydrides for hydrogen storage and compression applications *Mater. Today Proc.* **5** 10470–8
[12] Galvis E A R, Leardini F, Ares J R, Cuevas F and Fernandez J F 2020 Experimental behaviour of a three-stage metal hydride hydrogen compressor *J. Phys.* **2** 034006
[13] Yadav T P, Kumar A, Verma S K and Mukhopadhyay N K 2022 High-entropy alloys for solid hydrogen storage: potentials and prospects *Trans. Indian Natl Acad. Eng.* **7** 147–56
[14] Somo T R, Lototskyy M V, Yartys V A, Davids M W and Nyamsi S N 2023 Hydrogen storage behaviours of high entropy alloys: a Review *J. Energy Storage* **73** 108969
[15] Kumar A, Abu Shaz M, Mukhopadhyay N K and Yadav T P 2024 Phase transformation of AB5 to AB2 type phase on substitution of Mn with Zr in TiVCoNi (ZrxMn2-x) (x = 0, 0.3, 0.6, 1.0) high entropy alloys *Mater. Chem. Phys.* **318** 129291
[16] Fashu S, Lototskyy M, Davids M W, Pickering L, Linkov V, Tai S, Renheng T, Fangming X, Fursikov P V and Tarasov B P 2020 A review on crucibles for induction melting of titanium alloys *Mater. Des.* **186** 108295
[17] Li R, Zhu Y, Tang R, Wu D, Zeng L, Zhou Q and Liu J 2024 Optimized hydrogen storage properties of Ti–Zr–Mn–VFe-based alloys by orthogonal experiment for upscaled production *Mater. Chem. Phys.* **319** 129338
[18] Lee S 2000 Effects of boron and carbon on the hydrogenation properties of TiFe and Ti1.1Fe *Int. J. Hydrog. Energy* **25** 831–6
[19] Kostov A and Friedrich B 2006 Predicting thermodynamic stability of crucible oxides in molten titanium and titanium alloys *Comput. Mater. Sci.* **38** 374–85
[20] Zhang H R, Tang X X, Zhou L, Gao M, Zhou C G and Zhang H 2012 Interactions between Ni-44Ti-5Al-2Nb-Mo alloy and oxide ceramics during directional solidification process *J. Mater. Sci.* **47** 6451–8
[21] Davids M W, Lototskyy M, Malinowski M, van Schalkwyk D, Parsons A, Pasupathi S, Swanepoel D and van Niekerk T 2019 Metal hydride hydrogen storage tank for light fuel cell vehicle *Int. J. Hydrog. Energy* **44** 29263–72
[22] Friedrich B 1994 Large-scale production and quality assurance of hydrogen storage (battery) alloys *J. Mater. Eng. Perform.* **3** 37–46
[23] Larson A C and Von Dreele R B 2004 General structure analysis system (GSAS) *Report LAUR 86–748* (Los Alamos)
[24] Bobet J-L, Chevalier B and Darriet B 2000 Crystallographic and hydrogen sorption properties of TiMn2 based alloys *Intermetallics* **8** 359–63
[25] Troitzsch U, Christy A G and Ellis D J 2005 The crystal structure of disordered $(Zr,Ti)O_2$ solid solution including srilankite: evolution towards tetragonal ZrO_2 with increasing Zr *Phys. Chem. Miner.* **32** 504–14
[26] Martín-Sedeño M C, Marrero-López D, Losilla E R, León-Reina L, Bruque S, Núñez P and Aranda M A G 2005 Structural and electrical investigation of oxide ion and proton conducting titanium cuspidines *Chem. Mater.* **17** 5989–98
[27] Jones F W 1941 Particle size measurement by the x-ray method *J. Sci. Instrum.* **18** 157–8
[28] Hassanzadeh-Tabrizi S A 2023 Precise calculation of crystallite size of nanomaterials: a review *J. Alloys Compd.* **968** 171914
[29] Pearson W B 1972 *The Crystal Chemistry and Physics of Metals and Alloys* (Wiley)

Supplementary Information

To the article "Effect of preparation routes on the performance of a multi-component AB_2-type hydrogen storage alloy", by Moegamat Wafeeq Davids, Tayla Chirie Martin, Pavel V. Fursikov, Mikhail V. Zhidkov, Igor I. Khodos, Simbarashe Fashu and Mykhaylo V. Lototskyy

S1. Details of the XRD studies

The alloys phase composition was determined by XRD (Rigaku Minflex diffractometer) using Cu-Kα radiation ($\lambda1$=1.5406 Å, $\lambda2$=1.5444 Å, $\lambda2/\lambda1$=0.5, 2θ=15–90°). The XRD data was further processed by Rietveld full-profile analysis using GSAS software [S1] and the following reference data:

- C14-AB_2 Laves phase intermetallic ($Ti_{0.95}Zr_{0.05}Mn_2$) [S2]:
  - space group *P*6_3/mmc (194);
  - *a*=4.826 Å, *c*=7.921 Å, *V*=159.8 Å^3;
  - Atom coordinates:
    4 (Ti+Zr) in 4f, *x/a*=1/3, *y/b*=2/3, *z/c*=0.063;
    2 Mn1 in 2a, *x/a*=0, *y/b*=0, *z/c*=0;
    6 Mn2 in 6h, *x/a*=0.828, *y/b*=0.672, *z/c*=1/4.
- (Ti,Zr)O_2 mixed oxide [S3]:
  - space group *P*bcn (60);
  - *a*=4.7447 Å, *b*=5.0119 Å, *c*=5.4925 Å;
  - Atom coordinates:
    4 (Ti+Zr) in 4c, *x/a*=0, *y/b*=0.2015, *z/c*=1/4;
    8 O in 8d, *x/a*=0.270, *y/b*=0.399, *z/c*=0.429.
- La_2TiO_5 [S4]:
  - space group *P*nma (62);
  - *a*=11.0092 Å, *b*=3.9433 Å, *c*=11.4063 Å;
  - Atom coordinates:
    4 La1 in 4c, *x/a*=0.13583, *y/b*=1/4, *z/c*=0.06133;
    4 La2 in 4c, *x/a*=0.09589, *y/b*=1/4, *z/c*=0.71482;
    4 Ti in 4c, *x/a*=0.19216, *y/b*=1/4, *z/c*=0.37112;
    4 O1 in 4c, *x/a*=0.4915, *y/b*=1/4, *z/c*=0.60163;
    4 O2 in 4c, *x/a*=0.22631, *y/b*=1/4, *z/c*=0.53397;
    4 O3 in 4c, *x/a*=0.26388, *y/b*=1/4, *z/c*=0.8757;
    4 O4 in 4c, *x/a*=0.28146, *y/b*=1/4, *z/c*=0.23028;
    4 O5 in 4c, *x/a*=0.03816, *y/b*=1/4, *z/c*=0.32966.

When refining peak profile parameters, the GSAS Constant Wavelength (CW) X-ray profile function 2 was used. This function is commonly used for the refinement of X-ray powder diffraction data for Bragg-Brentano geometry [S1]. A standard α-Al_2O_3 sample was used to determine the instrumental contribution into peak profile parameters. During refinements, the instrument-dependent Gaussian profile parameters (GU, GV and GW) were fixed (kept the same as for the Al_2O_3 standard), and only two Lorentzian profile parameters were refined: LX (size broadening) and LY (strain broadening). The crystallite size was calculated using the formula presented in the GSAS manual [S1]:

$$b = \frac{18000\,K\,\lambda}{\pi\,X};$$

where b is the crystallite size in Å, X is the Lorentzian size broadening equal to the fitted profile parameter LX, λ= 1.5406 Å is a wavelength of Cu-Kα radiation, and K=0.9 is the Scherrer constant.

The refined XRD patterns including as-measured (I(obs)) and calculated (I(calc)) intensities, their difference (Obs–Calc) and the fitted background (I(bkg)), along with the peak positions of the constituent phases (bottom ticks), are presented in Figures S1–S3.

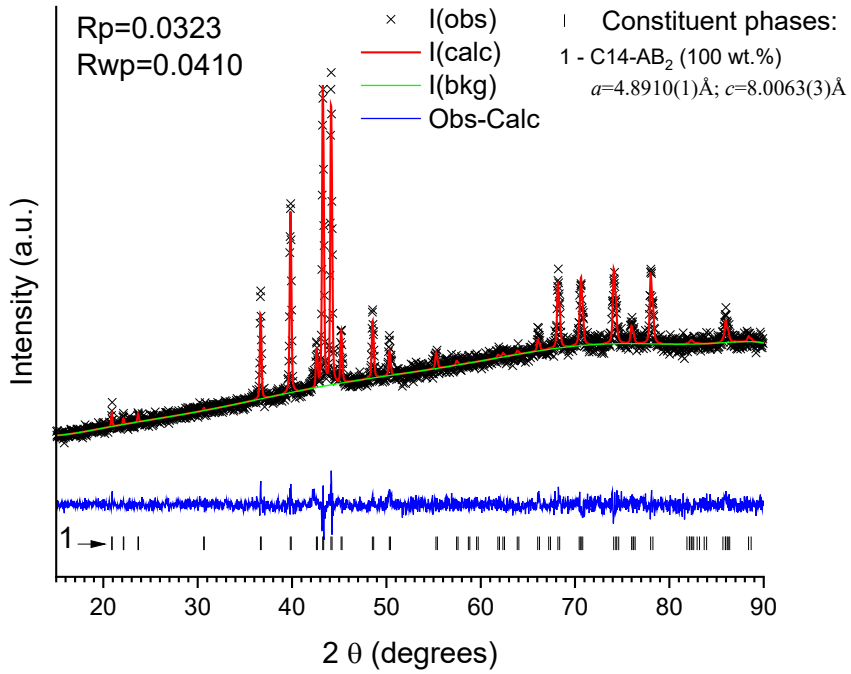

Figure S1. Refined XRD pattern of the arc-melted sample

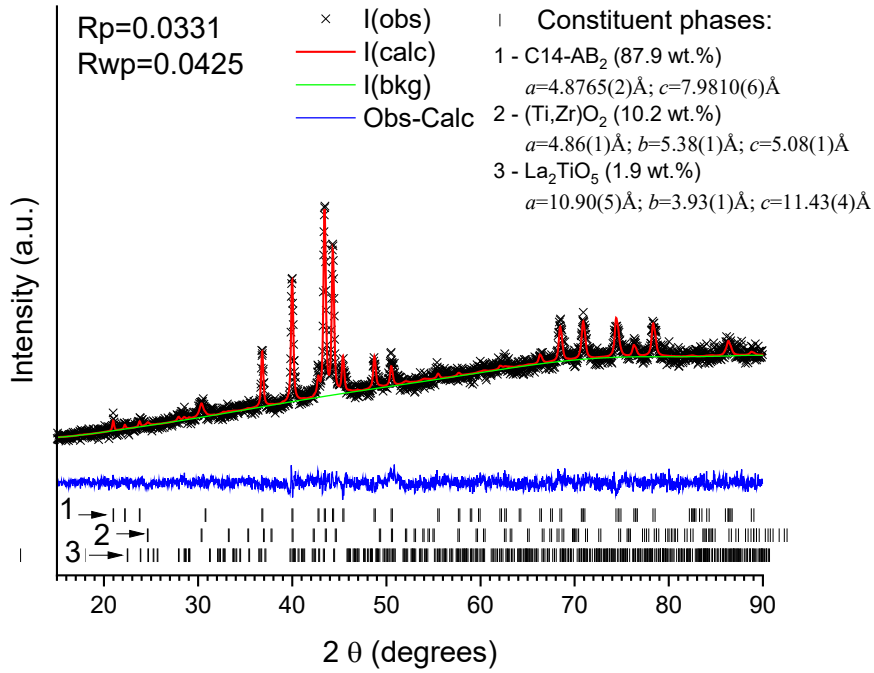

Figure S2. Refined XRD pattern of the sample induction-melted in alumo-silica crucible

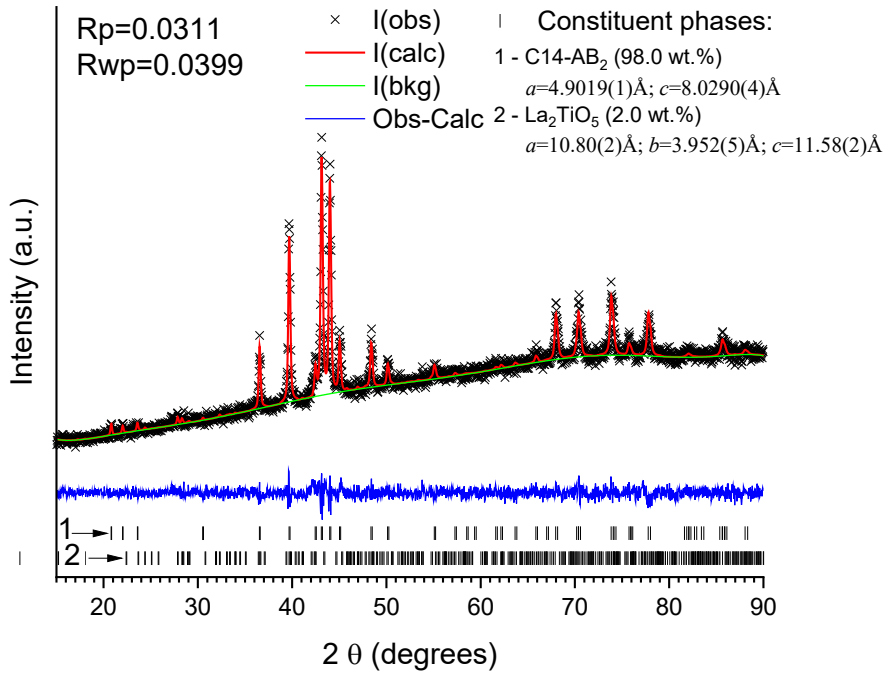

Figure S3. Refined XRD pattern of the sample induction-melted in graphite crucible

S2. Details of the TEM/SAED studies

Alloy: C14-$Ti_{0.85}Zr_{0.15}Mn_{1.22}Ni_{0.22}Cr_{0.2}V_{0.3}Fe_{0.06}$

Samples studied:

No. 1: Arc-melted;

No. 2: Induction-melted, Alumo-Silica crucible lined with Y_2O_3;

No. 3: Induction-melted, Graphite crucible lined with Y_2O_3.

For the induction-melted samples the starting charge additionally contained 1 wt.% of deoxidiser (lanthanum metal).

Fine powders of the samples were prepared by the manual grinding in agate mortar. A small fraction of the sample powder was deposited, using ultrasonic dispersant, onto substrate (copper mesh covered with electrically conductive amorphous film).

JEOL JEM-2100 electron microscope at the accelerating voltage of 200 kV was used.

Note that distance measurements on the SAED patterns when using scale bar were correct only in the horizontal direction. Therefore, for the processing of the SAED patterns we used metric correction calculated using the patterns of reference sample (gold).

General views of all three samples were similar. An example is shown in Figure S4.

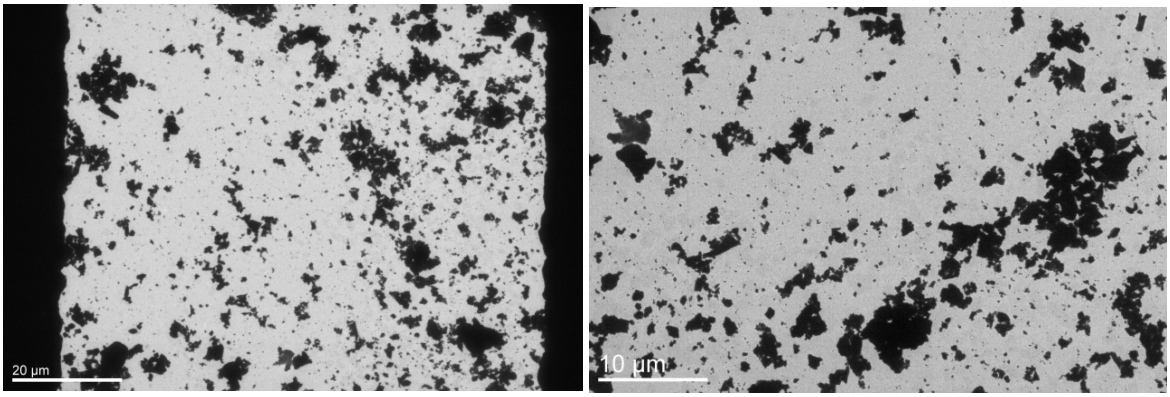

Figure S4. Typical low-resolution TEM image of the sample powder

The SAED patterns taken from the areas containing several separate particles are shown in Figures S5–S7. The patterns exhibit presence of both rings and spots testifying about mainly polycrystalline state of the particles some of which, however, contains monocrystalline blocks.

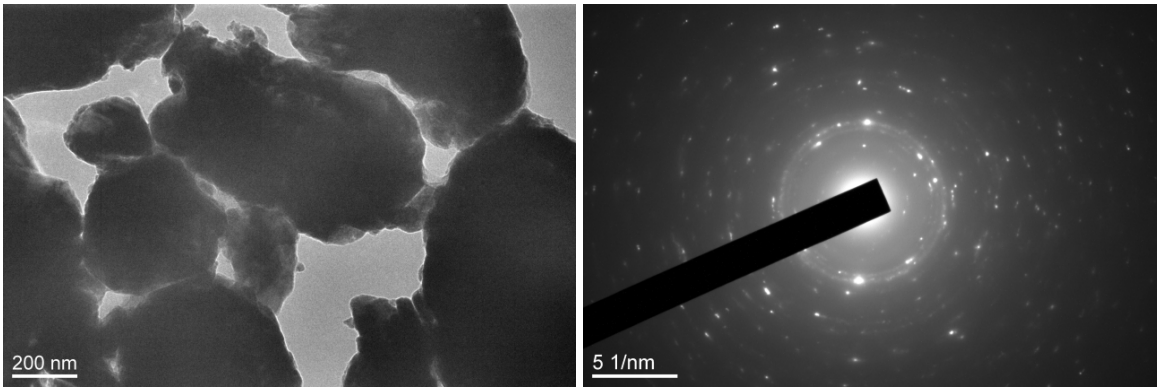

Figure S5. TEM image (left) and the corresponding SAED pattern (right) of sample No. 1

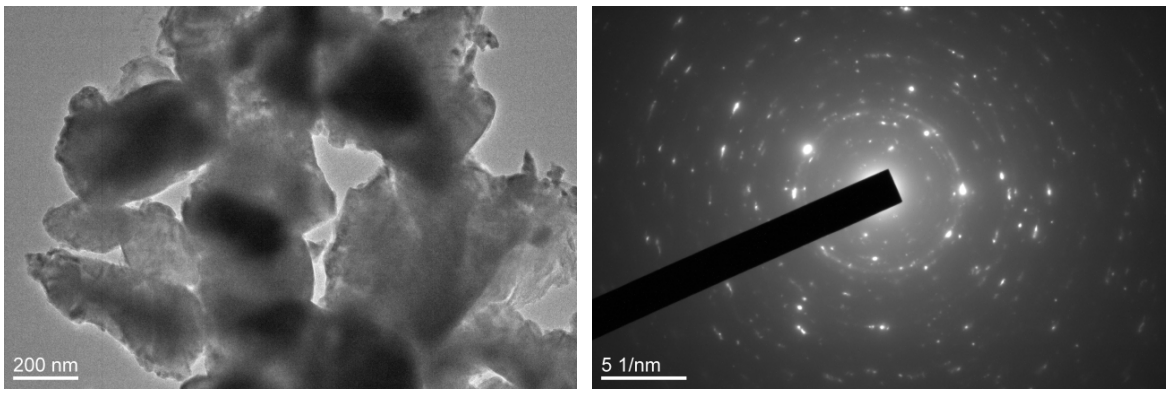

Figure S6. TEM image (left) and the corresponding SAED pattern (right) of sample No. 2

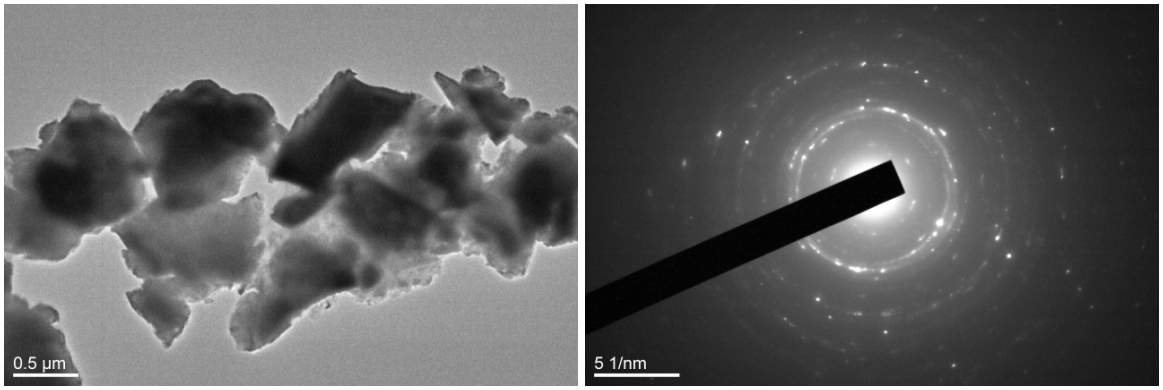

Figure S7. TEM image (left) and the corresponding SAED pattern (right) of sample No. 3

The separate completely polycrystalline particles (see Figures S8,S9) are absent in sample No. 3. The separate particles which include monocrystalline blocks are shown for samples No. 2 (Figure S10) and No. 3 (Figure S11).

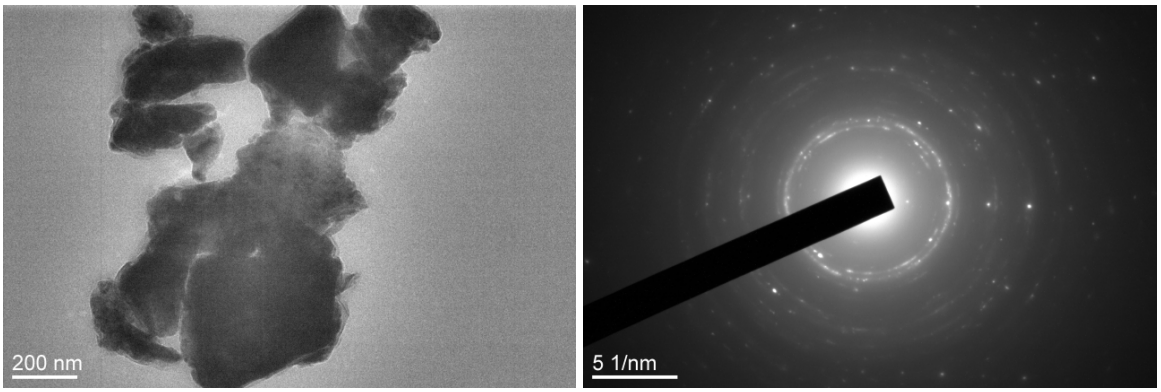

Figure S8. TEM image (left) and the corresponding SAED pattern (right) of separate particles of sample No. 1

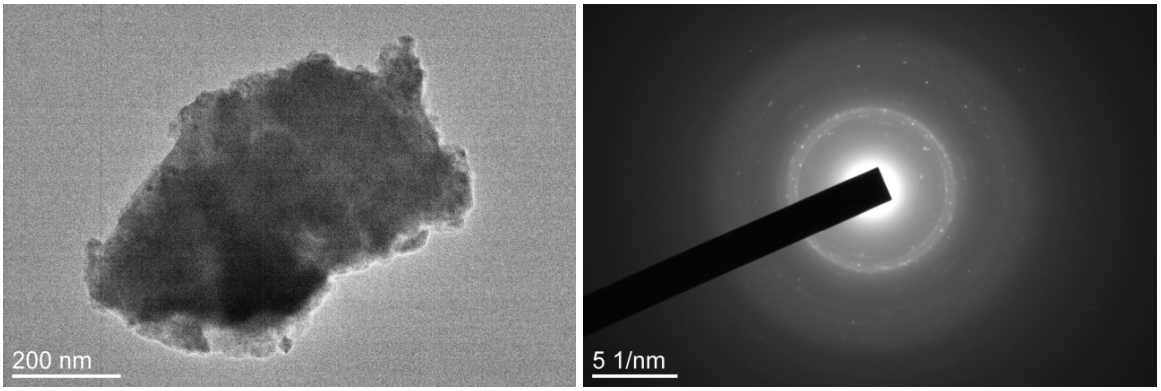

Figure S9. TEM image (left) and the corresponding SAED pattern (right) of separate particles of sample No. 2

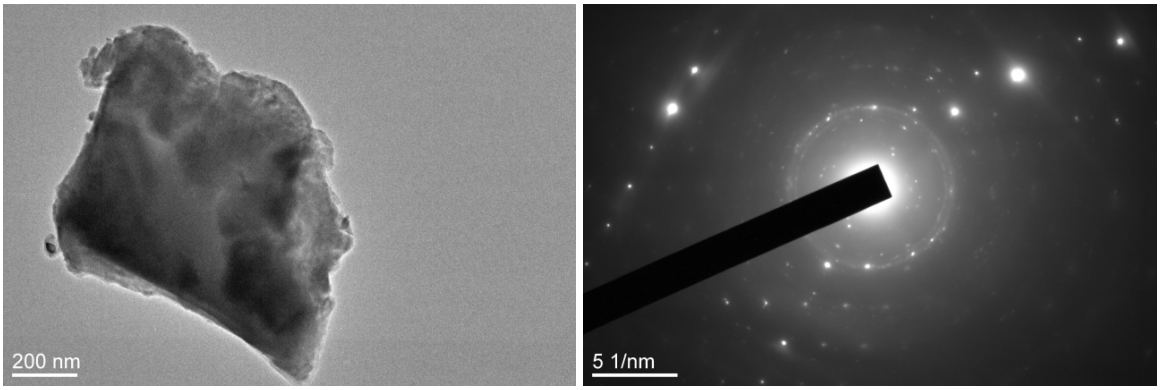

Figure S10. TEM image (left) and the corresponding SAED pattern (right) of separate particles of sample No. 2

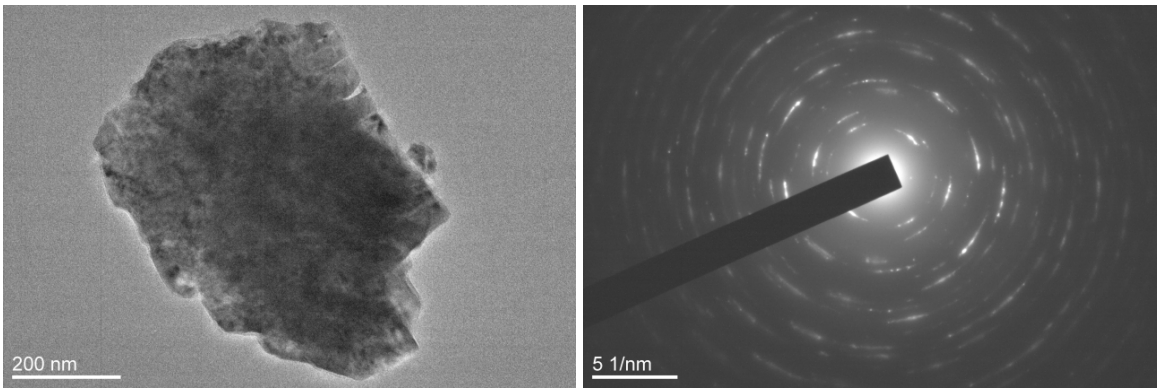

Figure S11. TEM image (left) and the corresponding SAED pattern (right) of separate particles of sample No. 3

All three samples exhibit presence of separate almost completely monocrystalline particles which for sample No. 3 have the high degree of crystallinity (Figure S12) while others – for samples No. 1 (Figure S13) and No. 2 (Figure S14) – are characterised by the poorer crystallinity.

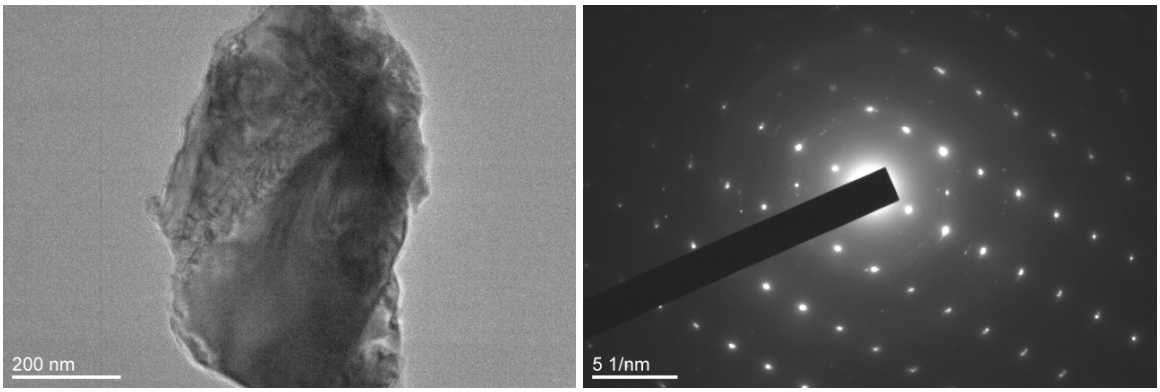

Figure S12. TEM image (left) and the corresponding SAED pattern (right) of separate particles of sample No. 3

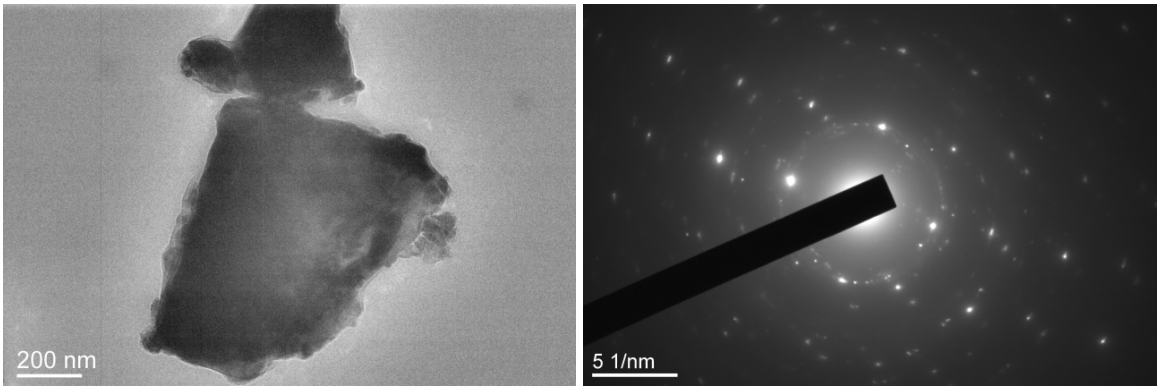

Figure S13. TEM image (left) and the corresponding SAED pattern (right) of separate particles of sample No. 1

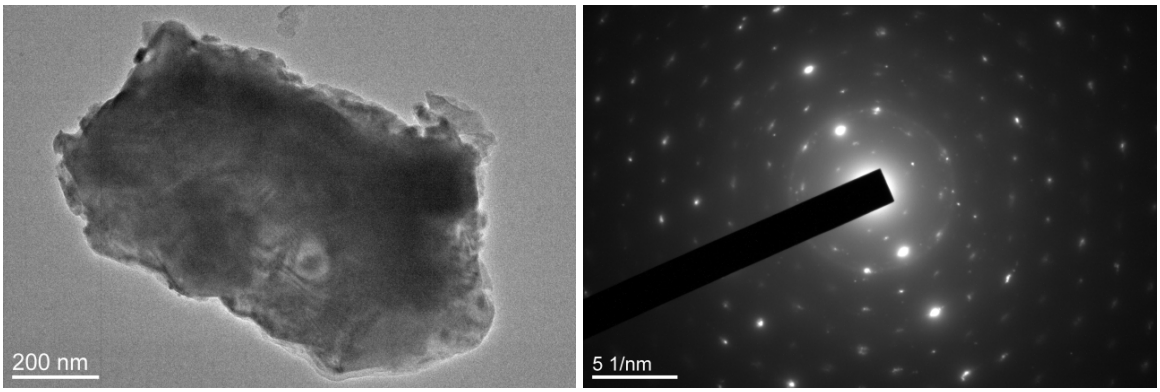

Figure S14. TEM image (left) and the corresponding SAED pattern (right) of separate particles of sample No. 2

The SAED patterns for all the samples exhibit presence of the major phase C14-AB_2 in a good correspondence with XRD studies presented in Section S1 and Section 3.2 of the main text (see example for sample No. 2 in Figures S15, S16 and Table S1).

Of the impurity phases, only traces of La_2TiO_5 poorly crystallised monocrystals were found in sample No. 2 (Figure S17, Table S2). Low probability of occurrence of the corresponding reflections in SAED patterns taken from an area of ~1μm in diameter (Figure S15) is caused by the small content of this phase in the sample (~0.2 wt.% according to the XRD data). Other impurity phases detected by XRD were not found in the SAED patterns of the samples, most probably, due to combination of their nanocrystalline nature and low abundancies.

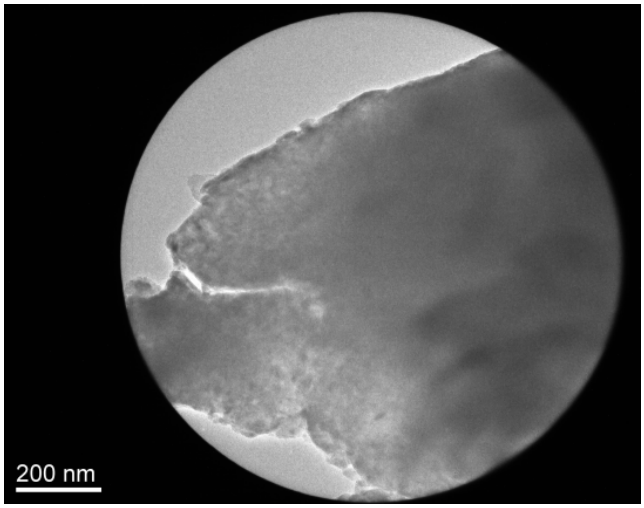

Figure S15. A selected area (sample No. 2) for taking electron diffraction patterns presented in Figures S16 and S17

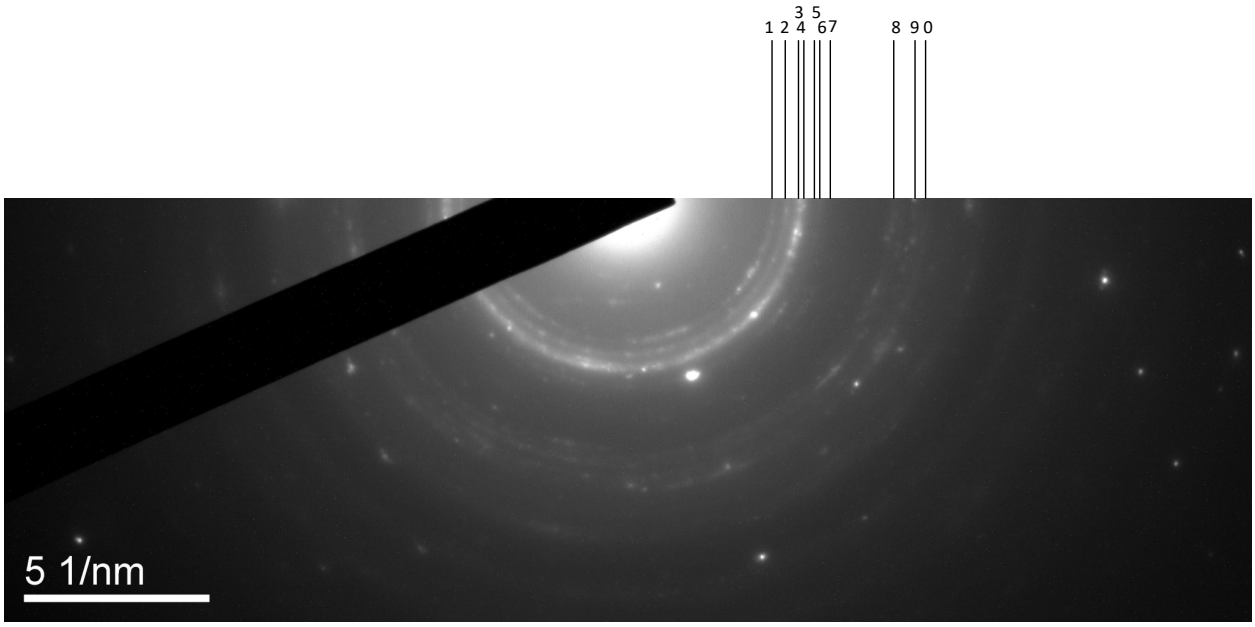

Figure S16. SAED pattern with indexed rings of the major C14-AB_2 phase (Table S1)

Table S1. Miller indexes of the rings of the major C14-AB_2 phase (Figure S16)

Number (*Figure S16*)	hkl
1	[110]
2	[103]
3, 4	[112], [201]
5	[202]
6	[104]
7	[203]
8	[302]
9	[205]
0	[220]

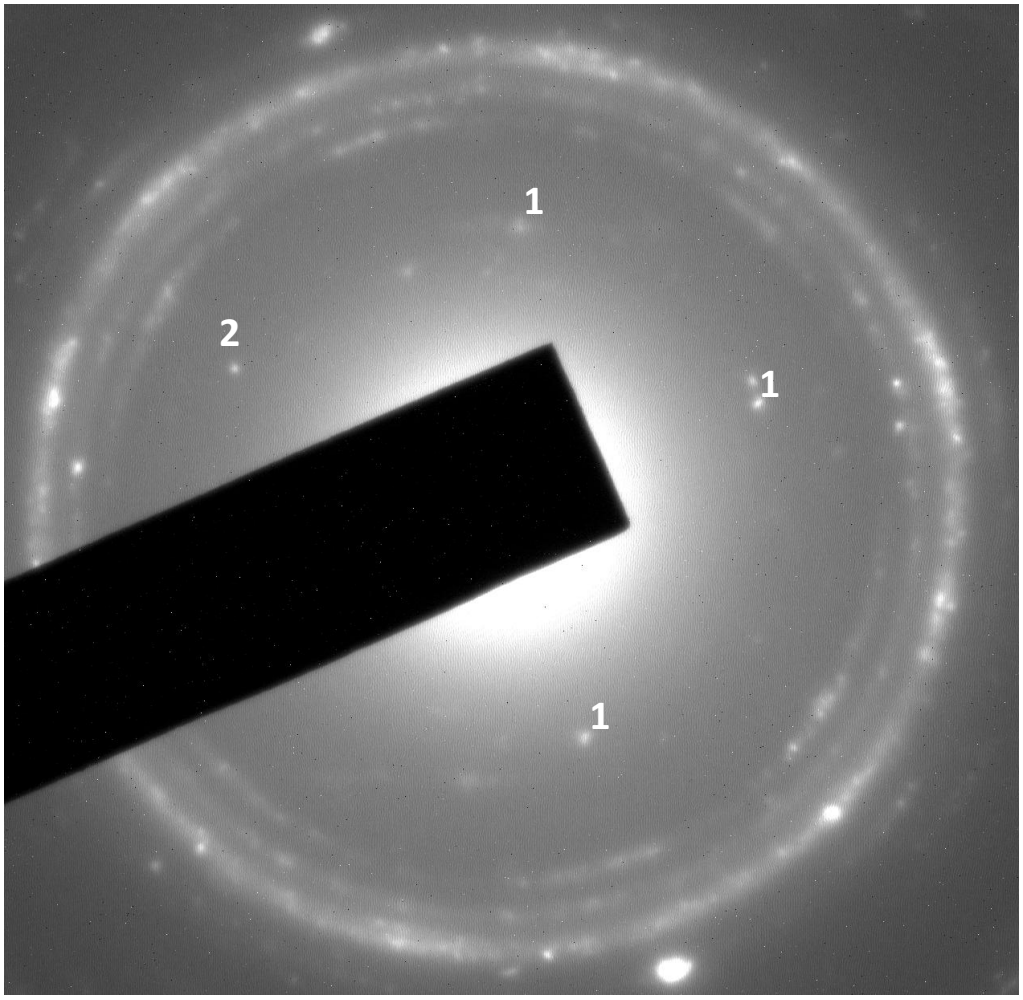

Figure S17. SAED pattern with indexed spots of the La_2TiO_5 impurity phase (Table S2)

Table S2. Miller indexes of the rings of the La_2TiO_5 impurity phase (Figure S17)

Number (*Figure S17*)	hkl
1	[130]
2	[201]

References

S1. Larson A C and Von Dreele R B 2004 General Structure Analysis System (GSAS), Report LAUR 86-748 (Los Alamos)

S2. Bobet J-L, Chevalier B and Darriet B 2000 Crystallographic and hydrogen sorption properties of $TiMn_2$ based alloys, Intermetallics (Barking) 8 359–63

S3. Troitzsch U, Christy A G and Ellis D J 2005 The crystal structure of disordered $(Zr,Ti)O_2$ solid solution including srilankite: evolution towards tetragonal ZrO_2 with increasing Zr, Phys Chem Miner 32 504–14

S4. Martín-Sedeño M C, Marrero-López D, Losilla E R, León-Reina L, Bruque S, Núñez P and Aranda M A G 2005 Structural and Electrical Investigation of Oxide Ion and Proton Conducting Titanium Cuspidines, Chemistry of Materials 17 5989–98